



Skeletonization method for vessel delineation of arteriovenous malformation

D. Babin^{a,*}, A. Pižurica^a, L. Velicki^b, V. Matić^c, I. Galić^d, H. Leventić^d, V. Zlokolica^e, W. Philips^a

^a imec-TELIN-IPi, Faculty of Engineering and Architecture, Ghent University, Belgium

^b Faculty of Medicine, University of Novi Sad, Serbia

^c Faculty of Technical Sciences, Singidunum University, Belgrade, Serbia

^d Faculty of Electrical Engineering, J.J. Strossmayer University Osijek, Croatia

^e Faculty of Technical Sciences, University of Novi Sad, Serbia



ARTICLE INFO

Keywords:

Image skeletonization
Image segmentation
Arteriovenous malformation delineation
3D rotational angiography
Medical image analysis

ABSTRACT

Cerebral arteriovenous malformation (AVM) presents a great health threat due to its high probability of rupture that can cause severe brain damage. Image segmentation alone is not sufficient to support AVM embolization procedure. In order to successfully navigate the catheter and perform embolization, the segmented blood vessels need to be classified into feeding arteries, draining veins and the AVM nidus. For this reason we address here the AVM localization and vessel decomposition problem. We propose in this paper a novel AVM localization and vessel delineation method using ordered thinning-based skeletonization. The main focus of vessel delineation is the delineation of draining veins since it is essential for the embolization procedure. The main contribution is a graph-based method for exact extraction of draining veins which, in combination with our earlier work on AVM detection, allows the AVM decomposition into veins, arteries and the nidus (with an emphasis on the draining veins). We validate the proposed approach on blood vessel phantoms representing the veins and the AVM structure, as well as on cerebral 3D digital rotational angiography (3DRA) images before and after embolization, paired with digital subtraction angiography (DSA) images. Results on AVM delineation show high correspondence to the ground truth structures and indicate potentials for use in surgical planning.

1. Introduction

Brain blood vessel visualization and analysis present crucial steps in diagnosis and treatment of cerebral aneurysms and arteriovenous malformations (AVM). For surgical planning it is crucial to precisely determine the positions and directions of vessels going in and out of the malformation. The AVM is composed of feeding arteries that supply the AVM with blood, the draining veins that drain the blood from the AVM and the nidus, which is an entangled vessel structure that poses a hemorrhage risk. One of the AVM treatment options is the embolization as a procedure of inserting glue into the blood vessels in order to occlude them and avoid their rupture. One of the main problems in AVM embolization is the accurate delineation of draining veins from other AVM vessels. The goal of the embolization is to occlude the nidus in such a way that the blood does not flow directly from arteries into the vein. The vein must remain

unsealed (clear blood passage) in order for the remaining blood to drain away as the nidus becomes blocked. On the other hand, an accidental occlusion of draining veins increases the risk of the nidus rupturing and causing a stroke. Therefore, it is essential to delineate the draining vein vessels inside the entangled structure of the AVM.

[11] give an overview of software for analysis of a 3-D vasculature, while [17] focus specifically on methods for AVM image analysis [28]. combine 3D digital rotation angiography (3DRA) and 2D digital subtraction angiography (DSA) for better visualization of AVMs and cerebral aneurysms. Similarly [21], combine 3D and 4D magnetic resonance angiography (MRA) images to obtain 4D blood flow visualization, while [29] use color-encoded 4D-hybrid MRA to perform classification of cerebral AVMs and intra-nidal flow. Some of the most popular methods for segmentation and visualization of cerebrovascular structures include direction-dependent level sets with vesselness measures [23] and ridge detection using seed points [12]

* Corresponding author.

E-mail addresses: daniilo.babin@ugent.be (D. Babin), aleksandra.pizurica@ugent.be (A. Pižurica), lazar.velicki@mf.uns.ac.rs (L. Velicki), vmatic@singidunum.ac.rs (V. Matić), irena@etfos.hr (I. Galić), hvoje.leventic@etfos.hr (H. Leventić), vzlokolica@uns.ac.rs (V. Zlokolica), wilfried.philips@ugent.be (W. Philips).

<https://doi.org/10.1016/j.complbiomed.2017.12.011>

Received 4 October 2017; Received in revised form 13 December 2017; Accepted 14 December 2017

[30]. introduced a blood vessel tracing method based on vesselness measures [24,45]. The *Vascular Modeling Toolkit* (VMTK) [2,42] is used for analysis of cerebral aneurysms [39]. proposed factor analysis approach for extraction of AVMs. The method of [40] uses principal component analysis (PCA) method on a sequence of dynamic X-ray CT images (obtained with contrast and opaque media) to identify the AVM area [16]. proposed a fractal analysis approach to quantify the vascular complexity of the AVMs. In our earlier work we used pixel profiling approach [9] and centerline analysis method [8] to detect and segment the AVM region. Albeit several accurate methods have been proposed to automatically analyze AVMs, only few of these methods address the internal AVM structure decomposition [12]. proposed a method for manual delineation of the AVM nidus with an interactive selection of feeding arteries and draining veins. The work of [22] delineates the AVM nidus, feeding arteries and draining veins, while assuming that the nidus exhibits a spherical structure and relying on specific values of vessel radii. The AVM segmentation on 3DRA using the information on the density of vessels and their variance combined with proximal manual tagging (starting from the nidus and followed by arteries and veins) was described in Ref. [14].

Centerline extraction is essential for examining tubular structures by allowing distance and radii calculations, best path determination and bifurcation detection. Vessel tracking methods perform region growing from seed points and track the propagation of the grown surface. The most common techniques are based on wave front propagation for ordered region growing [33], connected components evolution [13], generalized cylinder model [49], variational energy optimization [38] and the application of Dijkstra's shortest path algorithm [19] with the link costs derived from absolute difference of voxel gray values [32]. Skeletonization algorithms produce centerlines from binary or gray-scale images by extracting medial axis or ridges. The medial axis transform extracts centerlines by finding voxels equidistant to at least two object boundaries [10]. In Ref. [15], hierarchical curve-skeletons are extracted using repulsive force fields [1]. Other common techniques are based on radial basis functions and the gradient vector field [36], gradient vector flow [27] and visible repulsive force [48]. The most common gray-scale skeletonization approaches are based on anisotropic vector diffusion [49], conditional morphological erosion [37], thresholding prior to morphological erosion [20], pseudo-distance maps [31], the watershed algorithm [47] and planar images at angular rotations with unfiltered back-projection [26].

In our earlier work [6,7] we addressed the problem of detailed and accurate blood vessel and AVM segmentation using multi-scale and line-shaped operators. In this paper we build on our existing centerline analysis [8] and use the results of existing segmentation methods to delineate AVM structures. After the segmentation of the blood vessel tree is completed, we need to determine the location of an AVM (preferably in an automated way to omit user interaction). Together with the AVM localization, the AVM region needs to be extracted from the segmented images to perform vessel delineation into feeding arteries, draining veins and the AVM nidus. The vessel delineation should be performed semi-automatically using prior knowledge on vessel properties in 3DRA images.

We propose in this paper a novel method for AVM localization and decomposition using skeleton and graph analysis methods. The skeletonization will be performed using vessel radii and original gray voxel values as labels for ordered thinning. Similarly to [3], in order to efficiently analyze vessel structures, we introduce graph-type skeleton creation and analysis methods and use them to perform AVM localization and extraction. We design a novel vein extraction method based on skeleton analysis, which is robust to segmentation errors (segmentation "leaks"). Finally, we combine the listed methods into a complete AVM vessel delineation algorithm.

2. Materials and methods

In this paper we propose a novel method for AVM localization and extraction of the draining veins, which we further use for AVM

decomposition into the nidus, the draining veins and feeding arteries. We use ordered skeletonization to compute graph-type skeletons and perform vessel delineation. The following steps summarize our proposed method and give insight to our initial considerations about AVM vessel structure (see Fig. 1):

- Segmentation is the first step in blood vessel analysis, but it is not the focus of this work. In this work we use our segmentation method from Ref. [7], although other segmentation algorithms can also be used, providing they generate results of sufficient quality.
- Ordered skeletonization is performed on the distance transformed segmented image (distance values are input labels for ordered thinning). Alternatively, we will also use original voxel gray values to perform skeletonization. The skeletonized image is first transformed into a graph, and subsequently into a graph-type skeleton.
- Automatic localization and extraction of an AVM region. The AVM is an entangled blood vessel structure. The nidus of the AVM consists of high density of small intertwined vessels, represented by highly inhomogeneous voxel gray values in 3DRA images. This property will allow us to easily extract the AVM from the skeleton, since its region will be represented by nodes in which multiple links merge.
- Extraction of draining veins. The veins often (but not necessarily) constitute the largest blood vessels proximal to the AVM (they are dilated due to the missing capillaries that cause higher venous pressure). Therefore, the veins can be extracted by tracking large vessels and we perform this using a novel approach for merging highest cost links in the skeleton.
- Extraction of feeding arteries. Arteries contain higher concentration of contrast agent compared to veins, and smaller vessel radii compared to venous vessels. This yields higher voxel gray values along the centerline of the arterial vessels and lower gray values at vessel edges (this is due to the partial volume effect). Hence, original voxel gray values may be used as labels for the ordered thinning and the feeding arteries can be extracted as highest cost paths in the skeleton with original voxel gray values as link costs.

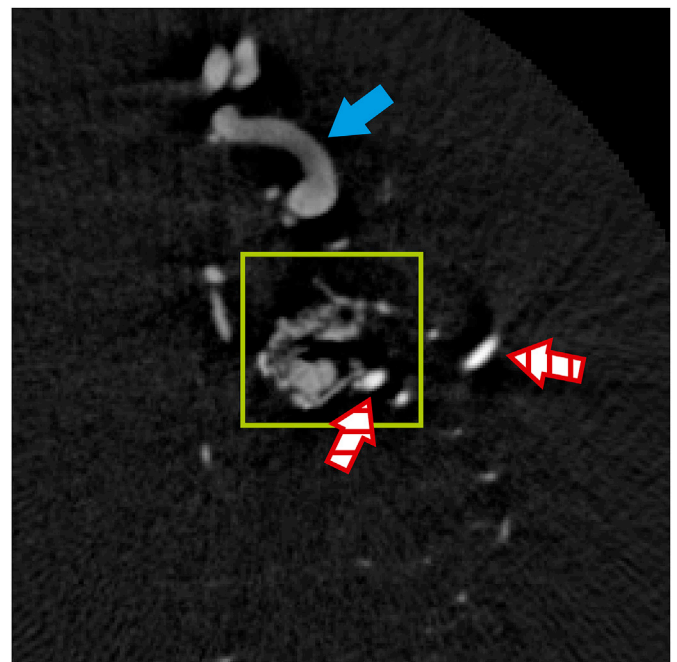


Fig. 1. : A 3DRA image slice of cerebral blood vessels. The AVM vessels (marked with a square) exhibit an undefined structure compared to the normal vessels. Arteries (striped arrows) are brighter due to higher density of contrast fluid. The veins (filled arrow) are the largest blood vessels with high inhomogeneity of voxel gray values.

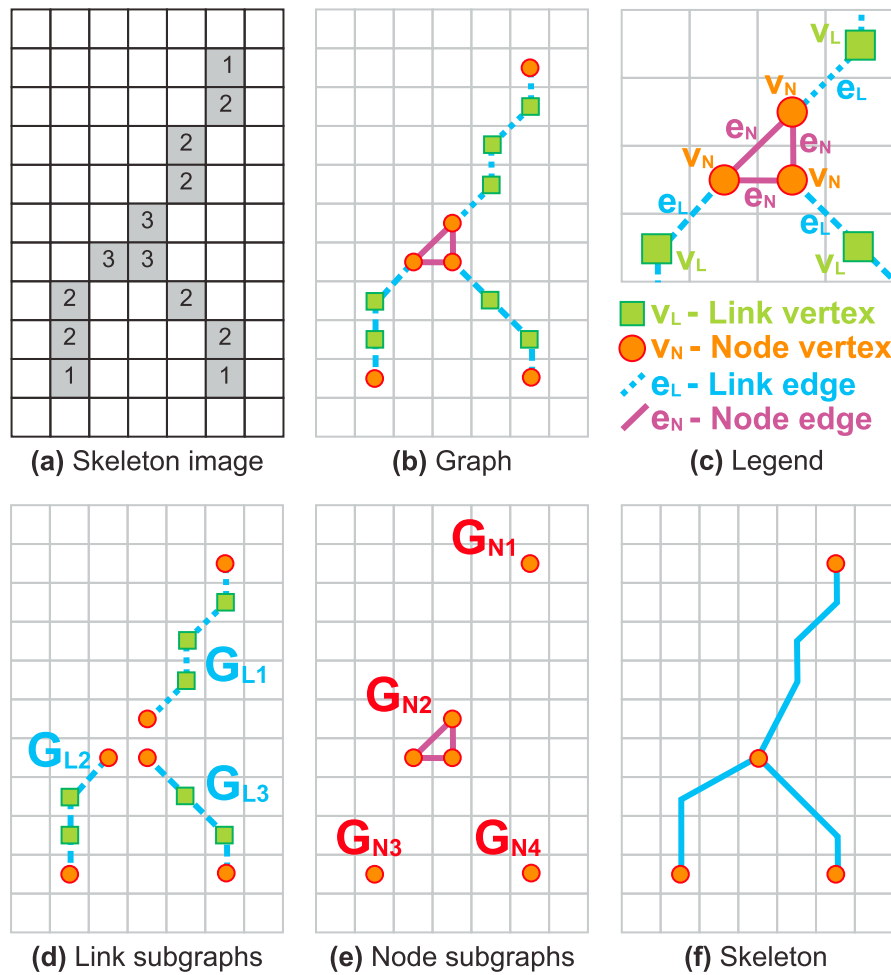


Fig. 2. Skeleton creation method. (a) Each voxel in the skeletonized image is labeled with its number of foreground neighbors. (b) A graph is created from the skeletonization image by turning each voxel into a graph vertex. (c) Classification of vertices and edges. (d) Link subgraphs G_L are formed from connected L-edges and will form links of the skeleton. (e) Node subgraphs G_N are formed from connected N-vertices and will form nodes of the skeleton. (f) The resulting skeleton shows that the bifurcation is defined by a single skeleton node and each branch with a single skeleton link.

2.1. Ordered skeletonization

The ordered skeletonization is an iterative thinning process of a segmented image, where voxels are removed in a predefined order. The goal is to obtain one voxel wide centerlines. The skeletonization consists of the following steps:

- Compute the squared Euclidean distance transform for each voxel in the segmented image (assign each foreground voxel a value of squared Euclidean distance to its nearest background voxel).
- Sort voxels into an ascending distance-value-ordered list.
- Iterating through the list remove redundant voxels from the segmented image using the voxel redundancy rule [5]: a voxel \mathbf{p} is considered *redundant* if all foreground (non-zero gray value) voxels in its 26-neighborhood constitute a single connected component.

The skeletonization changes a voxel label to background (zero gray value) if the voxel is redundant:

$$s(\mathbf{p}) = \begin{cases} 0, & \mathbf{p} \text{ is redundant} \\ g(\mathbf{p}), & \text{otherwise} \end{cases} \quad (1)$$

where $g(\mathbf{p})$ indicates the voxel gray value. The redundancy rule determines if a voxel can be removed from the segmented image while

preserving connectivity of all other voxels. However, the given voxel redundancy rule does not entirely preserve the topology of irregular shapes (such as AVMs) and creates holes in the skeletonization image. We emphasize here that we will use this property to our advantage, because it will enable us to automatically identify the AVM region.

2.2. Skeleton creation

In order to analyze the vessel structure, we need to convert the skeletonized image into a graph-type skeleton composed of nodes (to represent bifurcations and vessel ends) and links (to represent vessel branches). The skeleton creation is performed in following steps:

- Create a simple graph $G = (V, E)$, where V is a set of vertices and E is a set of edges, by considering every foreground voxel in skeletonized image as a graph vertex. The created graph is a simple graph, which means that it will not have any loop edges or multiple edges between adjacent vertices.
- Skeleton $S = (N, L, m, k)$ is created by partitioning the graph G into subgraphs that form skeleton nodes (N being the set of all nodes) and skeleton links (L is the set of all links) and maintaining the mapping functions m and k that map the nodes and links to their corresponding subgraphs. Ideally, each skeleton link should represent a vessel branch and each skeleton node should represent a bifurcation (or a

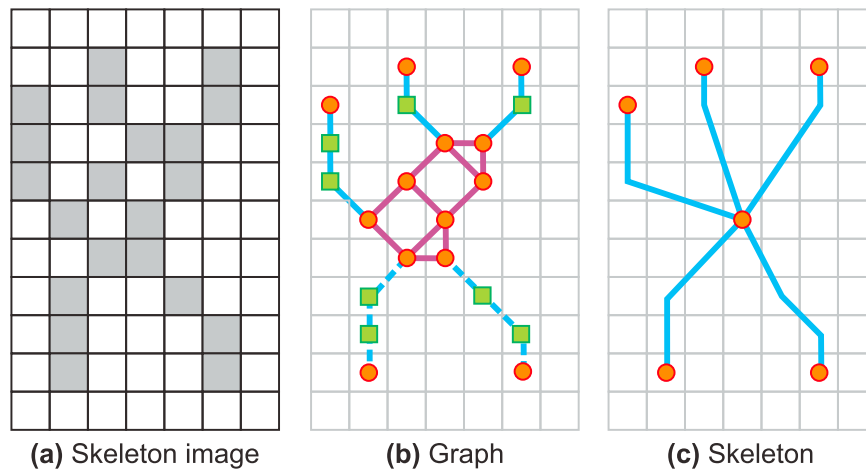


Fig. 3. The advantage of skeletons over graphs for malformation localization. (a) The skeletonized image of a malformation often contains “cavities” (caused by small intertwined vessels and inhomogeneities in voxel gray values). (b) Graph representation does not give an obvious indication of presence of a malformation. (c) Skeleton creation principle merges the region of “cavities” into a single skeleton node. The node is easily distinguishable since it contains numerous adjacent links.

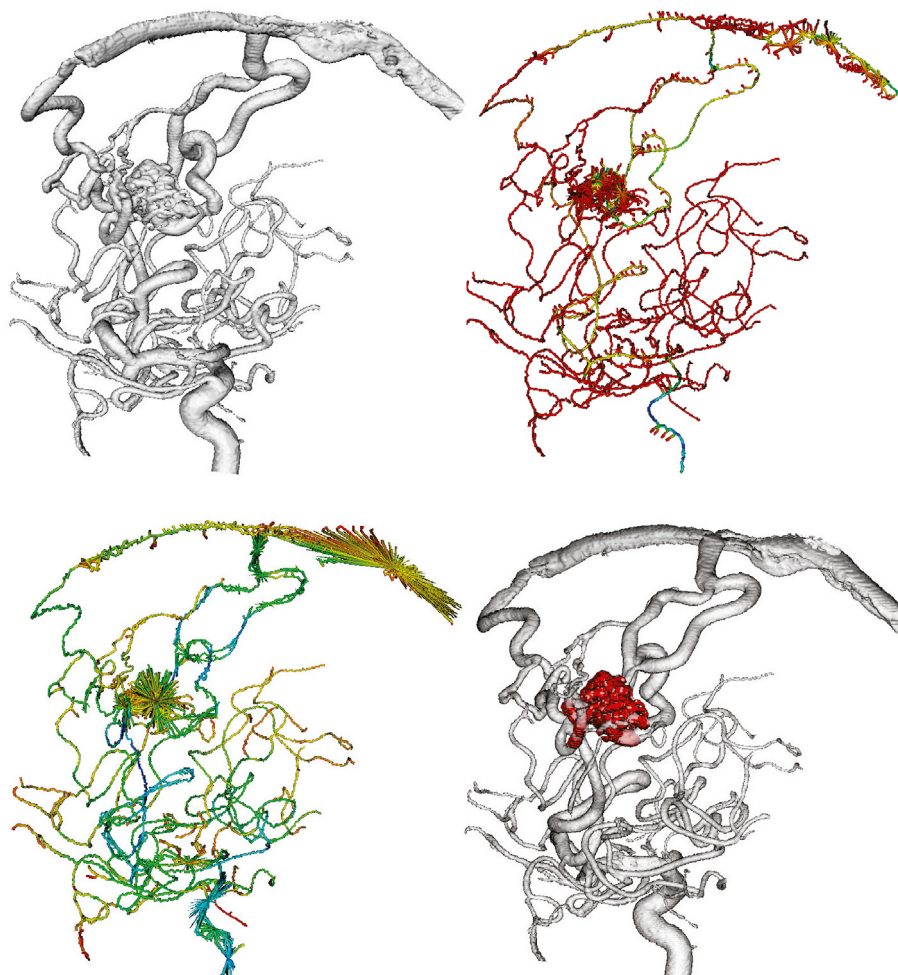


Fig. 4. Skeletonization and skeleton creation. Top row: the segmentation of the 3DRA cerebral blood vessels and the skeleton structure of the radii-based ordered skeletonization. Bottom row: skeleton structure of the gray value-based ordered skeletonization and the AVM region shown with the segmented vessels.

branch ending). For clarity we will use expressions “node” and “link” strictly for the skeleton structure and “vertex” and “edge” strictly for the graph structure.

A skeletonized image in Fig. 2a represents three blood vessel branches

with a single bifurcation, in which each foreground voxel is shown with a number of its neighboring foreground voxels. It should be observed that the bifurcation consists of voxels with 3 neighbors, while the branches consist of voxels with 2 neighbors and end with voxels that have only 1 neighbor. We convert the skeletonized image to undirected simple graph

$G = (V, E)$ by creating a vertex $v \in V$ from each foreground voxel and an edge $e = \{v_i, v_j\} \in E$ from each pair of adjacent vertices (26-connected voxels), as illustrated in Fig. 2b and c. Similarly as for voxels, each vertex is represented by its vertex degree $\deg(v)$, indicating the number of incident edges (equal to the number of neighboring voxels for corresponding voxel in the skeletonized image). We denote the vertices of degree 2 as *L-vertices* and vertices with any other non-zero degree value as *N-vertices* v_N . Vertices with degree value 0 are isolated vertices (that correspond to voxels without any foreground neighbors) and are not taken into account in skeleton construction. Similarly, we denote edges incident to at least one L-vertex as *L-edges* e_L and edges incident only to N-vertices as *N-edges* e_N (illustrated in Fig. 2b and c).

By classifying graph vertices and edges, we introduce a graph decomposition into subgraphs that represent vessel branches and bifurcations. If we denote a set of connected N-vertices v_N with V_N , we can define the node subgraph G_N as a graph induced by the vertex set V_N :

$$G_N = G[V_N]. \quad (2)$$

Fig. 2e shows that node subgraph G_{N2} corresponds to vessel bifurcation and will constitute node of the skeleton. Other nodes of the skeleton will be the graph vertices with vertex degree 1. The skeleton node created from node subgraph G_N will be represented by the geometric median of vertices the subgraph $V(G_N)$:

$$n = \text{med}_g(V(G_N)). \quad (3)$$

where $\text{med}_g(D)$ denotes the geometric median of a set of positions D as the position from the set with the minimum sum of distances to all other positions in the set:

$$\text{med}_g(D) = \arg \min_{p \in D} \left(\sum_{q \in D} d(p, q) \right), \quad (4)$$

where $d(p, q)$ denotes the Euclidean distance between the two positions. In order to maintain a mapping from the skeleton node to its subgraph, we define the *node mapping* function m :

$$m(n) = G_N. \quad (5)$$

If we denote a set of connected L-edges e_L with E_L , we can define the link subgraph G_L as a graph induced by the edge set E_L :

$$G_L = G[E_L]. \quad (6)$$

Fig. 2d shows that link subgraphs G_L correspond to vessel branches and will constitute links of the skeleton. A *skeleton link* l connects two skeleton nodes:

$$l = \{n_i, n_j\}. \quad (7)$$

In order to maintain a mapping from the skeleton link to its subgraph, we define the *link mapping* function k :

$$k(l) = G_L. \quad (8)$$

As with the node mapping function, with the link mapping function m we maintain the information from all the skeletonization voxels to allow reconstruction of the segmented vessels from the skeleton. The graph-type skeleton $S = (N, L, m, k)$ of the skeletonized image in Fig. 2a is illustrated in Fig. 2f. The mapping between the skeleton links (or nodes) and their corresponding subgraphs is important for the purpose of reconstructing vessels in the segmented image.

The most important advantage of skeleton representation over the simple graph representation is that blood vessel malformations can be easily detected. This is illustrated in Fig. 3, where the skeleton representation shows that multiple links merge in a single node (which is connected to numerous links). In case of the simple graph representation, this is not evident. Hence, it is reasonable to use skeletons for automatic

localization and extraction of malformations.

2.3. Localization and extraction of an AVM

In this subsection we propose a method for automatic localization and extraction of an AVM. As we illustrated in Fig. 3, the main advantage of skeletons over a simple graph representation of blood vessels is the possibility of easily detecting “porous” structures in skeletonized images that often correspond to blood vessel malformations. The skeleton in the top row of Fig. 4 is a result of the ordered skeletonization using vessel radii to define the thinning order. Color coding of links represents link costs derived from vessel radii values (inherited from skeletonization voxels) and range from red (for low values) to blue (for high values). It should be observed that “cavities” found in the skeletonization image are represented in the skeleton with nodes containing numerous links. The density of such nodes is the highest in the AVM. In other words, the AVM can be localized and extracted based on the location and density of nodes with high number of links. The skeleton in the bottom row of Fig. 4 is a result of the ordered skeletonization using original voxel gray values in the 3DRA image. Color coding of links represents link costs derived from original voxel gray values (inherited from skeletonization voxels) and range from red (for low values) to blue (for high values). It should be observed that density of nodes with high number of links is even more pronounced than in the case of the skeleton obtained using radii-ordered skeletonization. The reason is that the AVM nidus contains a lot of original voxel gray value inhomogeneities, besides the “cavities” contained in the skeletonization. Our most important observation is that the node with the highest number of links is positioned in the AVM, which allows us to automatically locate it:

$$n_{AVM} = \arg \max_{n \in N} (\deg(n)), \quad (9)$$

where $\deg(n)$ is a *node degree* representing the number of incident links of the node.

The whole AVM region can be represented with only a few nodes in which numerous links merge. We define the AVM region as the region of nodes connected to n_{AVM} that have more than 4 links (to avoid adding simple segmentation errors, which are often represented by nodes with 4 links):

$$N_{AVM} = \{n \mid n \in A(n_{AVM}), \deg(n) > 4\} \cup \{n_{AVM}\}, \quad (10)$$

where $A(n_{AVM})$ is a set of adjacent nodes of the node n_{AVM} . The sub-skeleton of the AVM is induced by the AVM node set:

$$S_{AVM} = S[N_{AVM}]. \quad (11)$$

The proposed AVM extraction principle is illustrated in the bottom row of Fig. 4, where the resulting segmented AVM region is shown as a part of the whole blood vessel tree. The AVM region is slightly over-estimated (it contains a part of the veins), which is a desired property for the draining veins extraction, as this serves only as an intermediate result in the delineation of veins, arteries and the nidus.

2.4. Delineation of draining veins

In this subsection we propose a novel method for extraction of draining veins of an AVM. The skeleton in the top row of Fig. 4 (obtained using vessel radii thinning order labels) shows that high cost values are found predominantly in the veins and to a small extent in the main feeding arteries. Hence, the veins can be extracted by tracing the paths with the largest link costs (in this case corresponding to the highest radii vessels) for known starting seed points. Starting positions of the draining veins are located within the AVM region, so we can use the location of the n_{AVM} node as the starting seed position for the draining veins. The end position for each draining vein will have to be supplied by the user.

In order to extract the path of the highest cost between 2 seed vertices

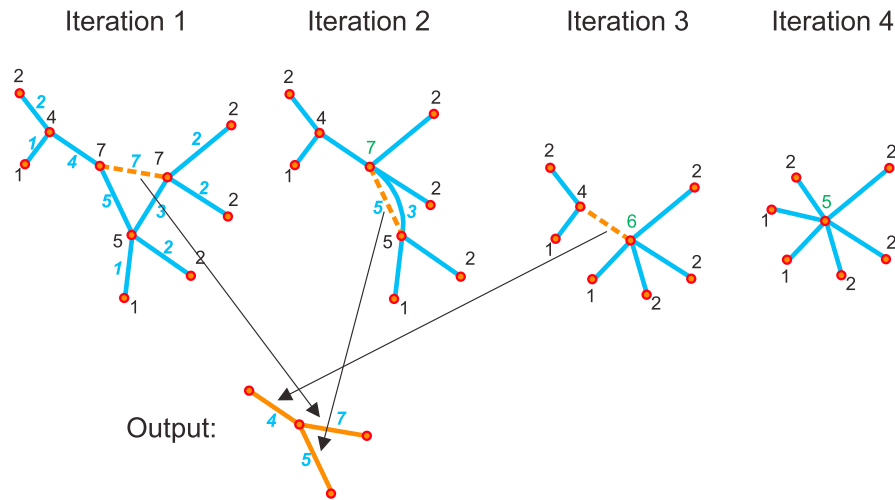


Fig. 5. Example of the highest cost vertex merging (HCVM) method. In the initialization step each vertex is assigned the highest cost of its incident edges. Afterwards, in each iteration we merge the highest cost vertex with its highest cost neighbor (through the highest cost edge, in case more edges between the vertices exist). A new vertex is created and assigned a cost equal to the average cost value of merged vertices. The contracted edge is added to the output graph. Loop edges are discarded. The algorithm stops when all edges are incident to a single vertex.

(or nodes) in the graph (or skeleton), we propose the approach of iterative *highest cost vertex merging* (HCVM). In other words, in every iteration the vertex with the highest cost will be merged with its adjacent highest cost vertex and their corresponding edge is removed from the processed graph and is recorded in the output graph. From the merged vertices a new vertex is created and assigned a cost equal to the average value of costs of merged vertices. The iterative edge removal is applied until all edges become incident (at that moment all edges will be connected to the same vertex). The detailed steps of the HCVM follow:

- Assign to each vertex the cost equal to the highest cost of all of its incident edges. This is an initial step and is performed only once.
- Find the vertex with the highest cost and its adjacent highest cost vertex.
- Contract their corresponding (highest cost) edge and add it to the output graph. If multiple edges exist, only the highest cost edge is added to the output graph.
- Remove all loop edges that were created by contraction in the previous step.
- Assign a cost to the newly created vertex as the average of costs of merged vertices.
- Stop iterating if all edges are connected to the same vertex. If not, repeat the method from the second step onwards.

Applying the HCVM method, the input graph contracts and output graph grows in size. With each iteration the processed graph G will become $G' = (V', E')$:

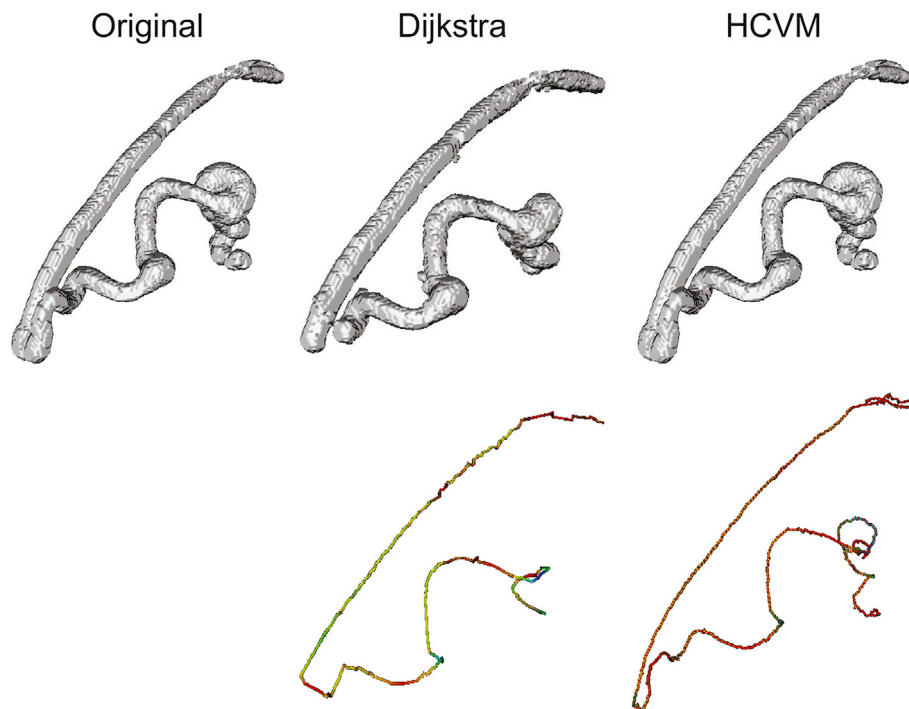


Fig. 6. Comparison of Dijkstra shortest path algorithm and HCVM method for blood vessel extraction. The skeleton and extracted vessel using the Dijkstra shortest path method are inaccurate (shortened at vessel bending points due to leaks in segmentation). Our HCVM method is able to surpass the incorrect segmentation problems.

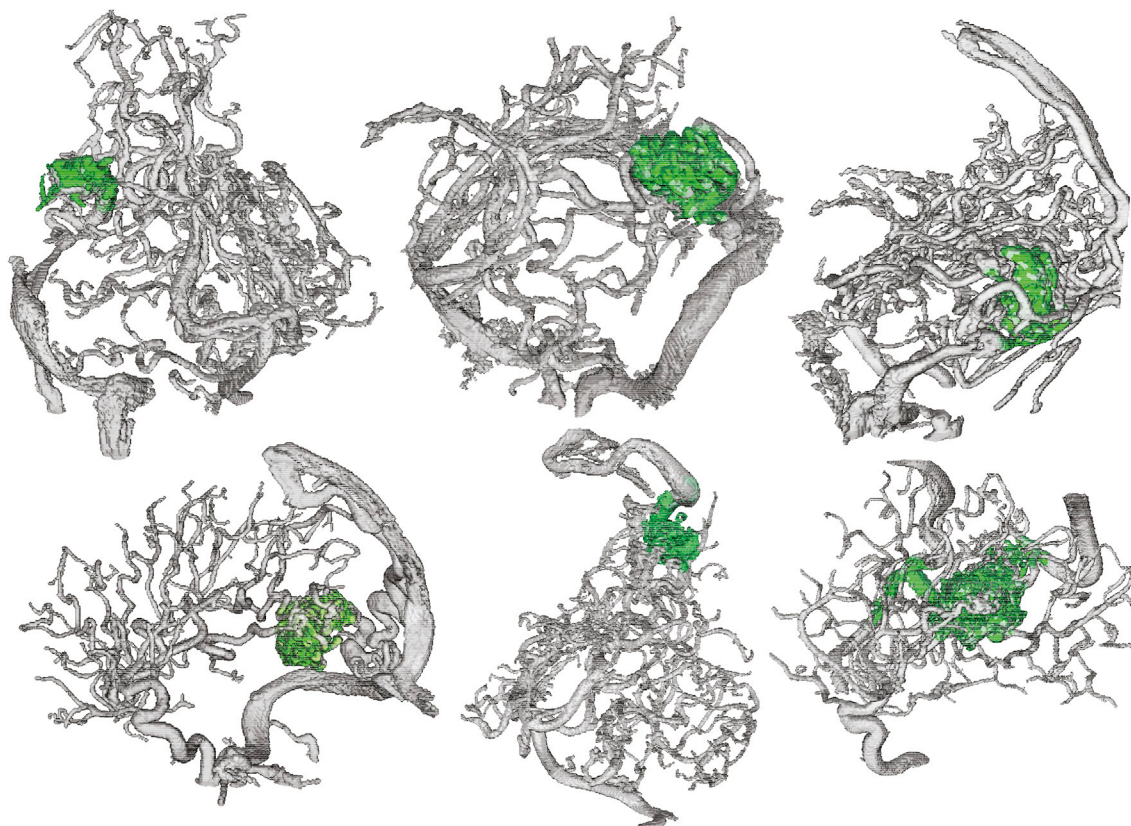


Fig. 7. Automatic localization of an AVM. In each case the AVM is correctly localized. The AVM region is slightly over-estimated, as required by the vein extraction method.

$$\begin{aligned} V' &= (V \setminus \{v_i, v_j\}) \cup \{v'\} \\ E' &= E \setminus \{e_{ij}\}, \end{aligned} \tag{12}$$

where V' and E' represent the new vertex and edge sets. Edge e_{ij} is the edge with the highest cost incident to vertices v_i and v_j . Vertex v' is the vertex obtained by merging of vertices v_i and v_j . The resulting graph $G_o = (V_o, E_o)$ grows with each iteration:

$$\begin{aligned} V_o &= V_o \cup \{v_i, v_j\} \\ E_o &= E_o \cup \{e_{ij}\}. \end{aligned} \tag{13}$$

The resulting graph will contain the paths with the highest costs, while all irrelevant low cost edges will be removed. An example of the proposed algorithm is shown in Fig. 5.

We want to point out an important property of the HCVM method. After the vertex merging, the cost of the new vertex will be the average

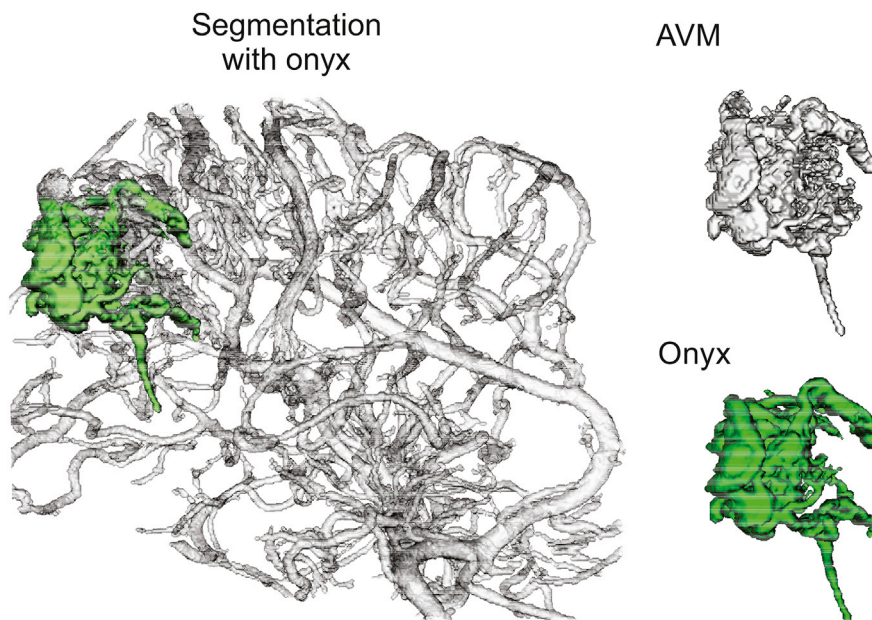


Fig. 8. The extracted AVM compared to the onyx cast, visualized with the vessel segmentation.

Table 1
Comparisons of the filled segmented onyx cast with the filled extracted AVM segmentation.

Onyx validation data set	1	2	3
Dice coefficient	0.83	0.77	0.81
Volume relative error (%)	10	18	13
AVM position distance (in voxels)	2.99	0.98	1.73

Table 2
Comparisons of the extracted AVM segmentation with manually segmented AVM region of an expert.

Data set	1	2	3	4	5	6	7	8
Dice coefficient	0.88	0.9	0.79	0.78	0.92	0.84	0.78	0.8
Volume relative error (%)	15	8	42	40	12	11	53	22

value of the costs of the merged vertices. With this approach we are able to surpass the problems in vessel extraction caused by flawed segmentation, i.e. low cost edges can be extracted if they are incident to high cost edges. On the other hand, if a vertex with a high cost merges with vertices with lower costs, the cost of the resulting vertex decreases and the merging process may be continued at another part of the graph.

In case the costs of edges have been assigned from the vessel radii, the HCVM will, in fact, extract the vessels with the highest radii (these are draining veins). The result of the HCVM will be a graph (or skeleton) containing the path between the seed points and the adjacent highest cost paths. By applying pruning on hierarchical skeleton we can allow the user to choose the number of remaining adjacent branches (next to the main seed point connecting path).

Fig. 6 illustrates the advantage of our HCVM method over Dijkstra's shortest path algorithm [19] for correct delineation of blood vessels. The depicted blood vessel has a lot of bending points, which cause segmentation errors (segmentation “leaks” due to the blood vessel “leaning” on

itself). The link costs used in this example for the Dijkstra's shortest path algorithm are inversely proportional to the vessel radii (lower radius value implies a higher link cost). The calculated best path skeleton and its corresponding segmentation are shortened at high bending angles of the vessel, where the segmentation leaks into the neighboring part of the vessel. On the other hand, our proposed HCVM method is able to accurately extract the centerline and reconstruct the segmented vessel.

2.5. Extracting the feeding arteries

In this subsection we explain the principle of extracting the feeding arteries. The skeleton in the bottom row of Fig. 4 is a result of ordered skeletonization using original voxel gray values in the 3DRA image. It should be observed that due to the high density of contrast agent in the feeding arteries, the highest link costs are also found in the feeding arteries. Therefore, we apply our HCVM method for extraction of feeding arteries by assigning original voxel gray values as edge (or link) costs. The only required user input are the starting seed points of the arteries.

3. Results and discussion

Clinical images used in our experiments were acquired on Siemens Axiom Artis scanner. The 3DRA images are sets of approximately 230 slices of dimensions 256 pixels × 256 pixels with spacing 0.48 mm × 0.48 mm and slice thickness of 0.48 mm.

3.1. Validation of the AVM localization and extraction

We validate our proposed method for localization and extraction of the AVM using 11 3DRA clinical data sets of cerebral AVMs. Correct localization was obtained for all data sets (one data set required discarding the first candidate and using the next best one as the AVM location, see Discussion subsection). Fig. 7 shows correct AVM

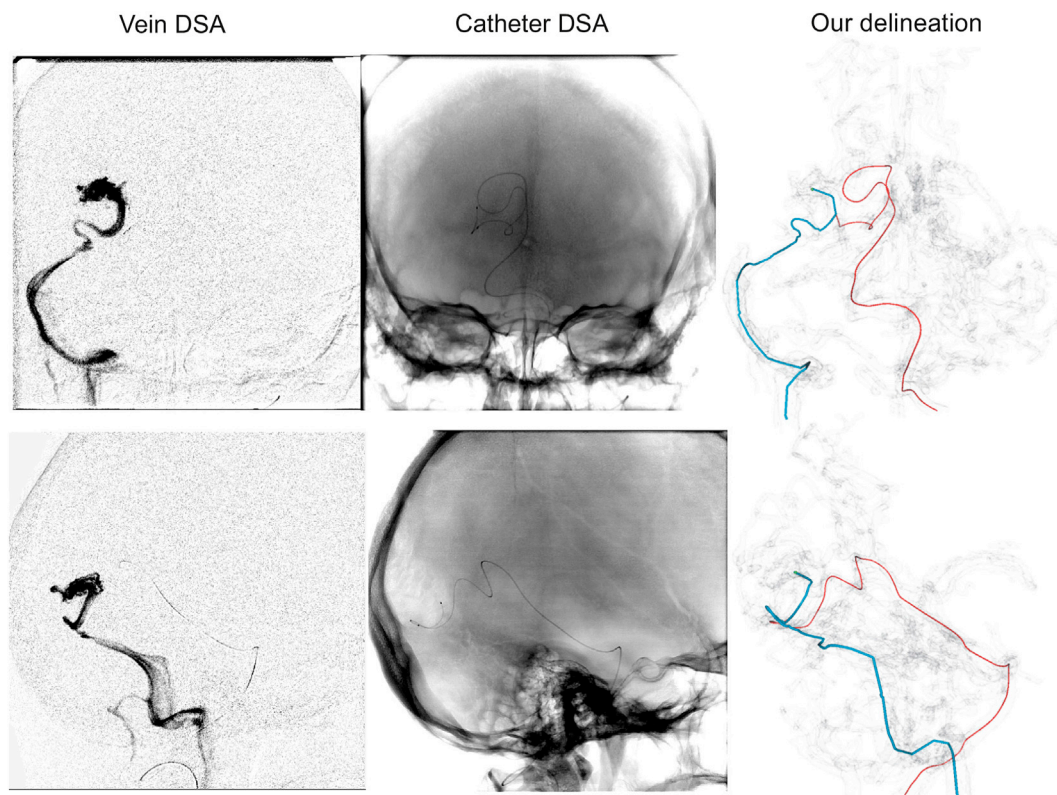


Fig. 9. Validation of arterial and venous best path calculation using DSA images of catheter and embolization. The extracted vein accurately shows the path of the injected contrast, while the arterial vessel precisely depicts the catheter position.

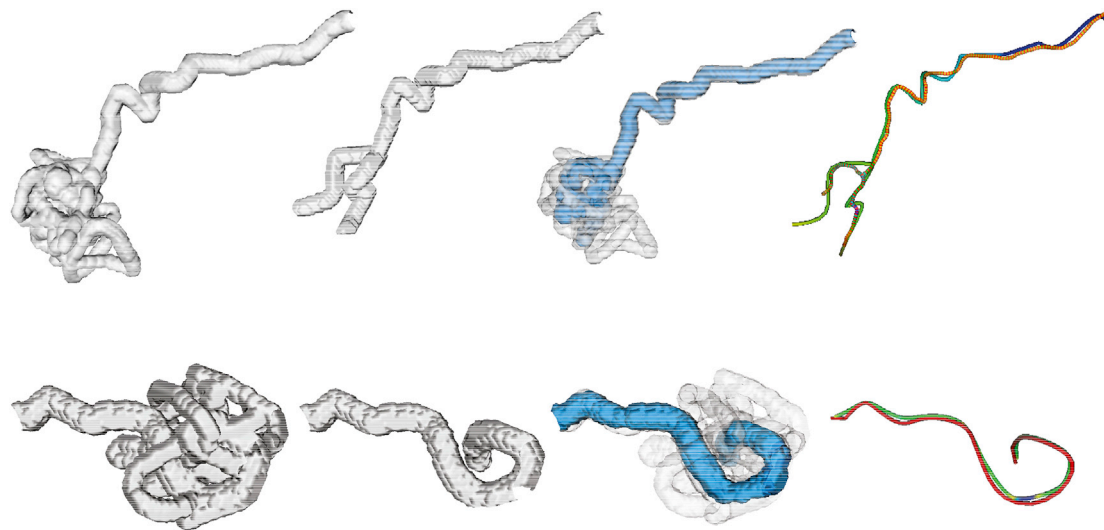


Fig. 10. Decomposition of the vein and nidus blood vessel phantom. First column: the vein and the AVM phantom are combined into a single region. Second column: the vein phantom. Third column: extracted vein overlaid on the whole blood vessel phantom. Fourth column: skeleton of the vein phantom and the extracted vein skeleton.

Table 3
Comparison of delineated and ground truth vein models (Dice coefficient) and skeletons (ratio of their lengths).

Vein & AVM	Dice	length ratio
Phantom 1	0,87	0.92
Phantom 2	0,84	0.86
Phantom 3	0,84	0.94

Table 4
Analysis of extracted veins and AVM regions for CURVES (C), projections (P) and threshold (T) based segmentation.

Robustness	T&C	C&P	P&T
Dice whole	0.874	0.829	0.848
Dice vein	0.933	0.899	0.909
Dice AVM	0.942	0.911	0.918
Vol % error whole	6.99	18.06	31.22
Vol % error vein	2.34	5.44	3.33
Vol % error AVM	2.97	14.37	13.41
AVM center distance (pixels)	0.308	0.737	0.338

localization results with slightly over-estimated AVM regions, as needed for the method that extracts the draining veins.

Further validation on clinical data is performed on 3 image pairs of blood vessels and onyx casts. The onyx cast images were acquired after the embolization procedure (see Fig. 8) and were segmented by thresholding (the threshold was easy to determine since there is a clear difference in range of pixel gray values in onyx and the surrounding region).

To suppress the influence of the segmentation algorithm on the validation, we apply a hole filling method to the segmented images of the onyx cast and the extracted AVM. For quantitative evaluation we use the Dice set similarity coefficient [18], defined as twice the ratio of the number of voxels in the intersection of two sets (the set of segmented voxels and the set of ground truth voxels) and the number of elements contained in both of them. The obtained results in Table 1 show good correspondence and low errors in AVM region estimation in terms of Dice coefficients, volume relative error and the distance between the AVM localization and onyx positions.

Manual segmentation of AVM regions (by an expert) was done for images which did not have the corresponding onyx cast image (images of onyx cast were not acquired after the embolization). The manual delineation was performed using multiple seed points as input for active contours in ITK-SNAP [50]. The resulting Dice coefficients and volume relative errors are shown in Table 2. The obtained results show good correspondence between the ground truth region and the extracted AVM region in terms of Dice coefficients and volume relative errors (for most of the data sets). The volume relative error is higher in 3 cases where the initial segmentation (the first step of the method) fails to provide good enough separation between the “touching” venous vessels of the AVM.

3.2. Validation of the vein extraction method

We validate our vein extraction method on 2 sets of clinical 3DRA images paired with DSA images of the catheter (in place for embolization) and DSA images of contrast injection (to determine the venous paths), as shown in Fig. 9. The extracted veins accurately represent the

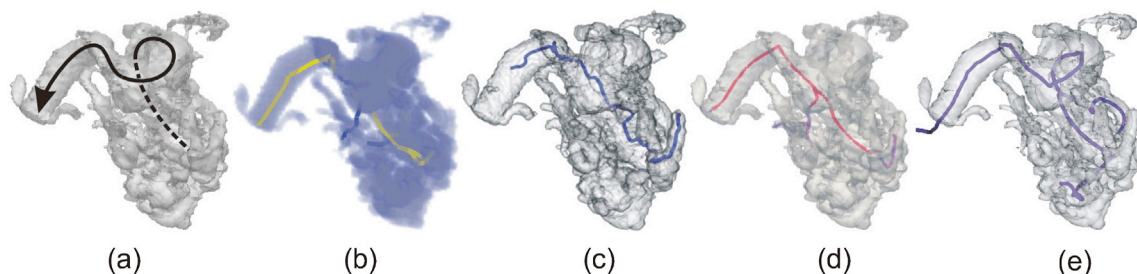


Fig. 11. Comparisons of the draining vein centerline extraction methods. (a) Manually extracted AVM region with the vein path indicated by an expert (drawn arrow). (b) Centerlines of vessel tracking algorithm [30] using a vesselness measure [45]. (c) Shortest path through the AVM for skeletonization using TubeTk [4]. (d) Centerlines obtained using VMTK [2,42]. For each extracted path, the vein is shorter than expected due to imperfect segmentation. (e) Our proposed method accurately extracts the venous centerline (despite existing segmentation “leaks”).

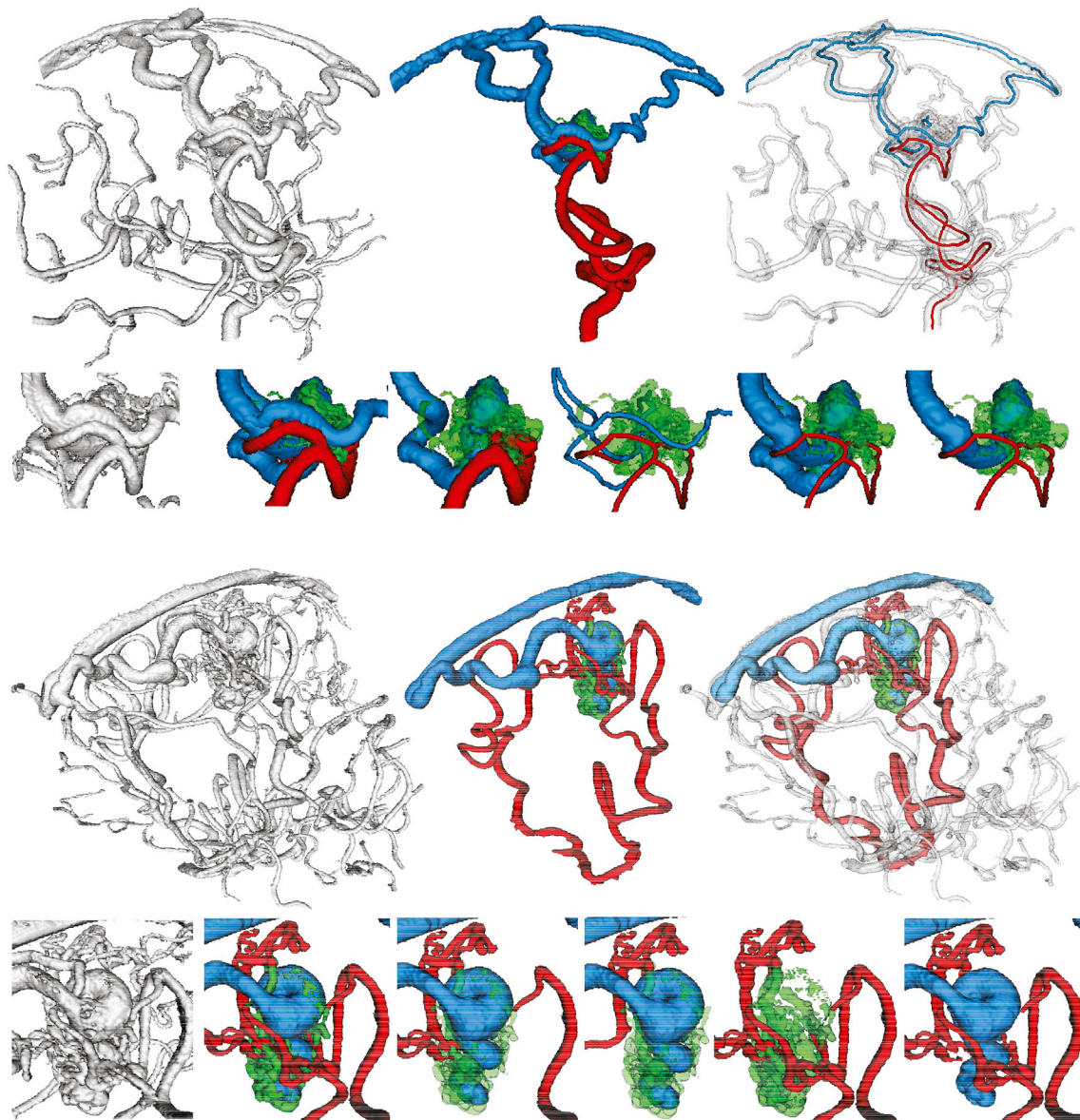


Fig. 12. Delineation result for two cerebral 3DRA data sets. The skeleton and the segmented region of veins are colored in blue, the feeding arteries are red and the nidus is green. The resulting delineation allows a surgeon to visualize selected vessels to obtain a better insight into the AVM structure. (For interpretation of the references to color in this figure legend, the reader is referred to the Web version of this article.)

path of the injected contrast in the DSA images. The extracted arterial vessels precisely depict the catheter path.

For further validation of our vein extraction method we created 3-D phantom data sets consisting of a separate model of an AVM and a venous blood vessel tree (see Fig. 10). The AVM phantom is simulated by generating a tube intertwined in a random fashion with randomly varying radii. The vein phantom is generated as a binary tree with random number of bifurcations, branch distribution, shape and radii. The final phantom was obtained by merging the AVM phantom and vein phantom at the place of venous vessel bifurcation (to be able to test if our method can correctly delineate the bifurcation in the AVM). The last two columns of Fig. 10 depict the extracted venous vessels overlaid on the original phantom and skeletons of original vein phantom and the extracted vein. It can be observed that the vein bifurcation was correctly delineated in the first phantom, while the curving of the vein was also accurately delineated in the second phantom. The quantitative comparison between the phantom vein and the extracted vein segmentation is given in Table 3. High Dice coefficient values indicate high accuracy of our decomposition method. The length ratio of delineated vein skeleton

and ground truth vein skeleton shows sufficient accuracy of centerline extraction.

One of the advantages of our proposed method using skeleton based vessel delineation is its robustness to used segmentation method. Table 4 shows comparison of results on AVM localization, AVM extraction and vein extraction for various segmentation methods: thresholding, Curve Evolution for Vessel Segmentation (CURVES) [35] and our line-shaped profiles [7]. We compare Dice coefficients for the segmentation of the whole blood vessel tree, extracted AVM and extracted veins for each pair of the listed segmentation methods. In each combination, the lowest Dice coefficients were obtained when comparing segmentation results of the whole blood vessel tree, which indicates high precision and robustness of our AVM and vein extraction methods. Similarly, the volume relative errors show highest volume differences in case of the whole blood vessel tree segmentation, and exhibit acceptable values for the vein and AVM extraction results. Finally, the results of AVM localizations were compared showing small distances between the calculated AVM centers.

We compared our method for delineation of veins with a centerline extraction method in Vascular Modeling Toolkit (VMTK) [2,42], shortest

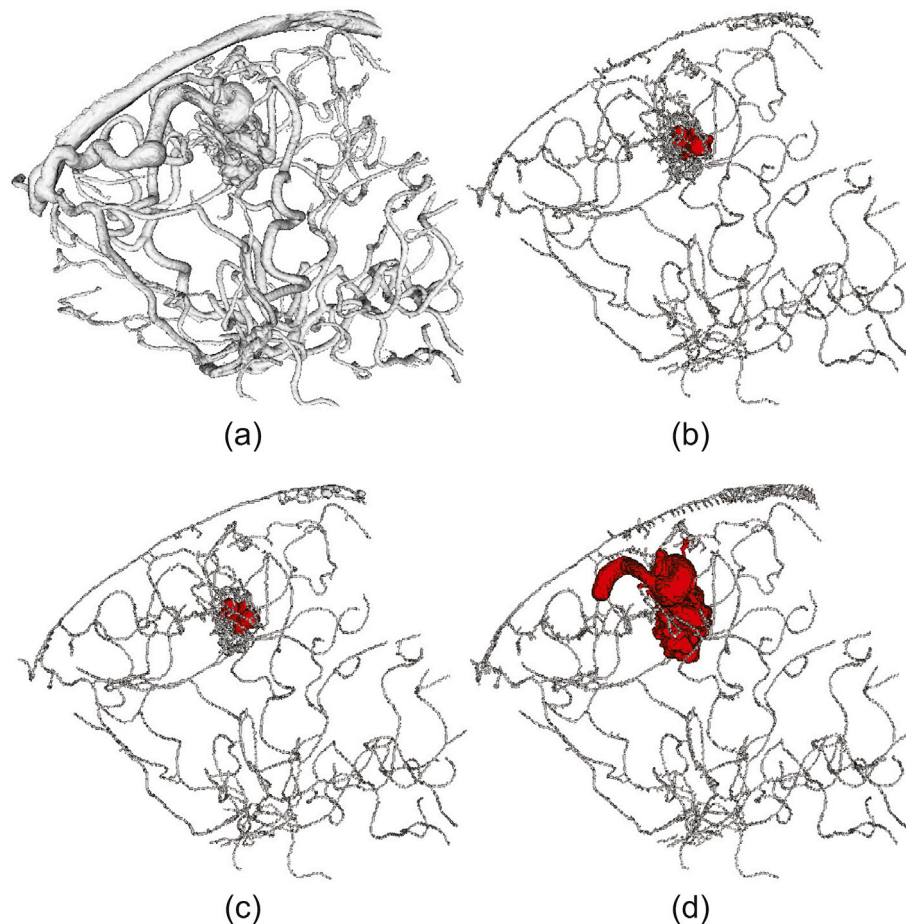


Fig. 13. Comparison of different skeletonization techniques for AVM localization and extraction. (a) Segmented blood vessels. (b) Result of the [25] skeletonization method (from Slicer3D application [43,44]) with extracted AVM. (c) Result of the [34] skeletonization method (from Fiji application [46]) with extracted AVM. (d) The result of our proposed skeletonization with the extracted AVM. Our method was able to accurately locate and extract the AVM region.

path through the AVM for skeletonization using TubeTk [4], and a vessel tracking tool [30] using vesselness measure [45] in BioImage Suite [41]. Fig. 11a shows the segmented AVM with the most probable path of draining veins indicated by an expert. Fig. 11b shows the vessel tracking result (BioImage Suite) obtained by placing multiple seed points in the veins and feeding arteries. The obtained result does not follow the indicated venous blood vessels, but instead shortens the centerline due to faulty segmentation. The TubeTk AVM skeletonization shortest path also yields a shorter venous path than expected (see Fig. 11c). Similarly, VMTK centerline extraction also shortens the venous centerline (see Fig. 11d). Due to the HCVM method our proposed algorithm accurately follows the venous centerline (see Fig. 11e).

3.3. Discussion

The result of the AVM vessel classification is shown in Fig. 12 for the whole blood vessel tree and with close-ups on the AVM. The obtained skeleton results show good correspondence to the real vessel anatomy, while clearly delineating the main vessels of the AVM. The AVM localization method is fully automatic, working accurately in over 90% of the cases for large and middle sized AVMs. Errors in AVM localization can occur in case large venous structures are visible with high inhomogeneity of voxel gray values, which in turn, constitute the skeleton node with the largest number of links (in the skeleton). In this case, the user can discard the incorrect localization and the skeleton node with next highest number of links will be selected as the AVM localization result. The vein extraction method (HCVM) is robust to segmentation errors (e.g. merged vessels in segmentation where vessels anatomically touch) for the cases

where the size (radius) of the region in which the vessels merge does not exceed the size (radius) of each of the merged vessels. Our method depends on the user to accurately place seed points in the veins that are connected to the AVM. In case a vein is not connected to the AVM nidus by the vessel segmentation, the vein will not be delineated from the nidus. To avoid incorrect delineation seed points can be placed close to the AVM region. Our method is also applicable in case of complex AVM structures that exhibit multiple draining veins, in which case multiple seed points for veins and arteries might need to be selected. For that reason the validation on simpler AVM phantom models as shown in Fig. 10 is applicable, since each of the multiple veins is treated separately. The proposed method is designed to tackle vessel delineation of AVMs with presence of an AVM nidus, but is not suitable for detecting other direct connections from arteries to veins (Arteriovenous Anastomoses).

The strength of our approach for localization of AVM vessels comes from the ordered skeletonization and our skeleton creation method. The used voxel redundancy rule is highly sensitive to inhomogeneities in voxel gray values, producing high number of cavities in the resulting skeletonization image. In turn, the cavities are represented in the skeleton by nodes with high number of incident links, which allows us to easily detect AVM vessels. This is not the case in skeletonization methods with sub-voxel precision, since they produce only few cavities, and hence, the AVM vessels are not as easily detectable. To illustrate the strength of our skeletonization method, we use different skeletonization methods in combination with our AVM delineation step (see Fig. 13). The result of [25] in Fig. 13b, shows that the localization of the AVM was accurately performed, but only a smaller part of the AVM is extracted. Skeletonization method of [34] also under-estimates the AVM region

(Fig. 13c). Using our proposed ordered skeletonization method we are able to accurately locate and extract the AVM (Fig. 13d).

The presented method is semi-automatic, with little user interaction required. Seed point placement is the only user input required to locate the arteries and veins (hence 2 or more input seeds are required). The method is highly robust to user input (seed point placement), especially if selected seed points are proximal to AVM region. The algorithm needs about 6 min to execute on a 2 GHz Intel Core 2 Duo processor with 8 GB of RAM. The skeletonization and graph-type skeleton creation take about 2 min to execute. Each of the remaining steps (localization and extraction of AVM, extraction of draining veins and feeding arteries) takes about 1 min to compute. Most of the computation time is spent on vessel reconstruction from the processed centerlines and the segmented image, while the actual skeleton processing in each of the extraction steps is performed with high efficiency (couple of seconds). It should be noted that the execution time depends on the image size and the number of vessels entering and exiting the AVM.

4. Conclusion

We designed a novel AVM decomposition method with an emphasis on delineation of draining veins. We introduced an approach for creating graph-type skeletons from skeletonized images. The proposed skeleton structures enabled us to perform automatic localization and extraction of AVM region. We designed a novel method for determining the highest cost path in the skeleton graph to perform extraction of draining veins. The proposed vein delineation method is able to extract the correct vessel paths even in presence of segmentation errors (“leaks”). The AVM localization and extraction methods were validated on 3DRA clinical data sets of cerebral vessels with the post-embolization scan of onyx cast. The method for extraction of draining veins was evaluated on 3-D phantom data sets and clinical 3DRA data sets with DSA images of catheter and embolization procedure. The robustness of our methods was evaluated using segmentation results of various segmentation methods. The results on accuracy and robustness of AVM localization and vessel delineation indicate possibility for surgical use. The designed application is semi-automatic requiring little manual user input to perform delineation.

Acknowledgement

The research described in this paper was not supported by any specific grant from funding agencies in the public, commercial, or not-for-profit sectors.

References

- N. Ahuja, J.H. Chuang, Shape representation using a generalized potential field model. *Pattern Analysis and Machine Intelligence*, IEEE Trans. 19 (1997) 169–176.
- L. Antiga, D. Steinman, Vmtk - Vascular Modeling Toolkit, 2006. <http://www.vmtk.org>. nn-nn.
- S. Aylward, J. Jomier, C. Vivert, V. LeDigaercher, E. Bullitt, Spatial graphs for intracranial vascular network characterization, generation, and discrimination, MICCAI (2005) 59–66.
- S. Aylward, D. Pace, A. Enquobahrie, M. McCormick, C. Mullins, C. Goodlett, P. Reynolds, Tubetk, Segmentation, Registration, and Analysis of Tubular Structures in Images, Kitware Inc., Clifton Park, 2012.
- D. Babin, J. De Bock, A. Pizurica, W. Philips, The shortest path calculation between points of interest in 3-d mri images of blood vessels, in: Annual Workshop on Semiconductor Advances for Future Electronics and Sensors, 11th, Proceedings, STW Technology Foundation, 2008, pp. 295–298.
- D. Babin, A. Pizurica, R. Bellens, J. De Bock, Y. Shang, B. Goossens, E. Vansteenkiste, W. Philips, Generalized Pixel Profiling and Comparative Segmentation with Application to Arteriovenous Malformation Segmentation. *Medical Image Analysis*, vol. 16, Elsevier, 2012, pp. 991–1002.
- D. Babin, A. Pizurica, J. De Vlyder, E. Vansteenkiste, W. Philips, Brain blood vessel segmentation using line-shaped profiles, *Phys. Med. Biol.* 58 (2013) 8041–8061.
- D. Babin, M. Spyrrantis, A. Pizurica, W. Philips, Skeleton calculation for automatic extraction of arteriovenous malformation in 3-d cta images, in: IEEE International Symposium on Biomedical Imaging, ISBI 2014, Beijing, China, 2014.
- D. Babin, M. Spyrrantis, A. Pizurica, W. Philips, L. Velicki, V. Zlokolica, Pixel profiling for extraction of arteriovenous malformation in 3-d cta images, in: ELMAR (ELMAR), 2014 56th International Symposium, IEEE, 2014b, pp. 1–4.
- H. Blum, et al., A transformation for extracting new descriptors of shape, *Models for the perception of speech and visual form* 19 (1967) 362–380.
- E. Bullitt, S. Aylward, Patient-specific vascular models for endovascular and open operative procedures, *Int. Congr.* 1247 (2002) 129–138.
- E. Bullitt, S. Aylward, E. Bernard, G. Gerig, Computer-assisted visualization of arteriovenous malformations on the home pc, *Neurosurgery* 48 (2001) 576–583.
- J. Carrillo, M. Orkisz, M. Hoyos, Extraction of 3d vascular tree skeletons based on the analysis of connected components evolution, in: A. Gagalowicz, W. Philips (Eds.), *Computer Analysis of Images and Patterns*, Springer Berlin, Heidelberg, 2005 volume 3691 of *Lecture Notes in Computer Science*, pp. 604–611.
- F. Clarençon, F. Maizeroi-Eugène, D. Bresson, F. Maingreaud, N. Sourour, C. Couquet, D. Ayoub, J. Chiras, C. Yardin, C. Mounayer, Elaboration of a semi-automated algorithm for brain arteriovenous malformation segmentation: initial results, *Eur. Radiol.* 25 (2015) 436–443.
- N. Cornea, D. Silver, X. Yuan, R. Balasubramanian, Computing hierarchical curve-skeletons of 3d objects, *Vis. Comput.* 21 (2005) 945–955.
- A. Di Leva, The fractal geometry of the brain: an overview, in: *The Fractal Geometry of the Brain*, Springer, 2016, pp. 3–12.
- A. Di Leva, M. Boukadoum, S. Lahmiri, M.D. Cusimano, Computational analyses of arteriovenous malformations in neuroimaging, *J. Neuroimaging* 25 (2015) 354–360.
- L.R. Dice, Measures of the amount of ecologic association between species, *Ecology* 26 (1945) 297–302.
- E.W. Dijkstra, A note on two problems in connection with graphs, *Numer. Math.* 1 (1959) 269–271.
- P. Dokladal, C. Lohou, L. Perrotton, G. Bertrand, A New Thinning Algorithm and its Application to Extraction of Blood Vessels, 1999.
- N. Forkert, J. Fiehler, T. Illies, D. Maller, H. Handels, D. Saring, 4d blood flow visualization fusing 3d and 4d mra image sequences, *J. Magn. Reson. Imag.* 36 (2012) 443–453.
- N. Forkert, T. Illies, E. Goebell, J. Fiehler, D. Saring, H. Handels, Computer-aided nidus segmentation and angiographic characterization of arteriovenous malformations, *Int. j. Comput. Assist. Radiol. Surg.* (2013) 1–12.
- N.D. Forkert, D. Saring, T. Illies, J. Fiehler, J. Ehrhardt, H. Handels, A. Schmidt-Richberg, Direction-dependent level set segmentation of cerebrovascular structures, in: *Progress in Biomedical Optics and Imaging*, 2011.
- A. Frangi, W. Niessen, K.L. Vincken, M. Vieregger, Multiscale vessel enhancement filtering, in: *Medical Image Computing and Computer-assisted Intervention-MICCAI'98*, Springer-Verlag, 1998, pp. 130–137.
- G. Gerig, T. Koller, G. Székely, C. Brechbuhler, O. Kubler, Symbolic description of 3-d structures applied to cerebral vessel tree obtained from mr angiography volume data, in: H. Barrett, A. Gmitro (Eds.), *Information Processing in Medical Imaging*, Springer Berlin/Heidelberg, 1993 volume 687 of *Lecture Notes in Computer Science*, pp. 94–111.
- C. Hanger, S. Haworth, R. Molthen, C. Dawson, Semiautomated skeletonization of the pulmonary arterial tree in micro-ct images, in: *Society of Photo-optical Instrumentation Engineers (SPIE) Conference Series*, pp. 510–516, 2001.
- M. Hassouna, A. Farag, On the extraction of curve skeletons using gradient vector flow, in: *Computer Vision, 2007. ICCV 2007. IEEE 11th International Conference on*, pp. 1–8, 2007.
- D. Hristov, L. Liu, J.R. Adler, I.C. Gibbs, T. Moore, M. Sarmiento, S. Chang, R. Dodd, M. Marks, H.M. Do, Technique for targeting arteriovenous malformations using frameless image-guided robotic radiosurgery, *Int. J. Radiat. Oncol. Biol. Phys.*, Elsevier 79 (2011) 1232–1240.
- T. Illies, N. Forkert, T. Ries, J. Regelsberger, J. Fiehler, Classification of cerebral arteriovenous malformations and intracranial flow patterns by color-encoded 4d-hybrid-mra, *Am. J. Neuroradiol.* 34 (2013) 46–53.
- M. Jackowski, X. Papademetris, L. Dobrucki, A. Sinusas, L. Staib, Characterizing vascular connectivity from microct images, in: J. Duncan, G. Gerig (Eds.), *Medical Image Computing and Computer-assisted Intervention MICCAI 2005*, Springer Berlin/Heidelberg, 2005, pp. 701–708.
- J.H. Jang, K.S. Hong, Detection of curvilinear structures and reconstruction of their regions in gray-scale images, *Pattern Recogn.* 35 (2002) 807–824.
- A. Kanitsar, D. Fleischmann, R. Wegenkittl, D. Sandner, P. Felkel, E. Groller, Computed tomography angiography: a case study of peripheral vessel investigation, in: *Visualization, 2001. VIS '01. Proceedings*, pp. 477–593, 2001.
- C. Kirbas, F. Quek, Vessel extraction in medical images by 3d wave propagation and traceback, in: *Bioinformatics and Bioengineering, 2003. Proceedings. Third IEEE Symposium on*, pp. 174–181, 2003.
- T.C. Lee, R. Kashyap, C. Chu, Building skeleton models via 3-d medial surface axis thinning algorithms, *CVGIP Graph. Models Image Process.* 56 (1994) 462–478.
- L. Lorigo, O. Faugeras, W. Grimson, R. Keriven, R. Kikinis, A. Nabavi, C.F. Westin, Curves: curve evolution for vessel segmentation, *Med. Image Anal.* 5 (2001) 195–206.
- W.C. Ma, F.C. Wu, M. Ouhyoung, Skeleton extraction of 3d objects with radial basis functions, in: *Shape Modeling International, 2003*, pp. 207–215, 2003.
- S.S. Mersa, A.M. Darwish, A new parallel thinning algorithm for gray scale images, in: *IEEE Nonlinear Signal and Image Proc. Conf.*, pp. 409–413, 1999.
- V. Mohan, G. Sundaramoorthi, A. Stillman, A. Tannenbaum, Vessel segmentation with automatic centerline extraction using tubular tree segmentation, in: *CI2BM09-MICCAI Workshop on Cardiovascular Interventional Imaging and Biophysical Modelling*, pp. 666–673, 2009.
- Y. Nyui, K. Ogawa, E. Kunieda, Extraction of arteriovenous malformation with factor analysis, in: *Image Processing, 2000. Proceedings. 2000 International Conference on*, IEEE. pp. 621–624, 2000.

- [40] Y. Nyui, K. Ogawa, E. Kunieda, A new approach to the visualization of intracranial arteriovenous malformation with principal component analysis, in: Nuclear Science Symposium Conference Record, 2000 IEEE, IEEE. pp. 23–11, 2000.
- [41] X. Papademetris, M. Jackowski, N. Rajeevan, M. DiStasio, H. Okuda, R.T. Constable, L. Staib, Bioimage Suite: an Integrated Medical Image Analysis Suite: an Update. Computer Software, Available from:<http://www.bioimagesuite.org>, 2006 (n/a, n/a–n/a.).
- [42] M. Piccinelli, A. Veneziani, D.A. Steinman, A. Remuzzi, L. Antiga, A framework for geometric analysis of vascular structures: application to cerebral aneurysms, *IEEE Trans. Med. Imag.* 28 (2009) 1141–1155.
- [43] S. Pieper, M. Halle, R. Kikinis, 3d slicer, in: Proceedings of the 1st IEEE International Symposium on Biomedical Imaging: from Nano to Macro 2004, IEEE International Symposium on Biomedical Imaging ISBI 2004. pp. 632–635, 2004.
- [44] S. Pieper, B. Lorensen, W. Schroeder, R. Kikinis, The na-mic kit: Itk, vtk, pipelines, grids and 3d slicer as an open platform for the medical image computing community, in: Biomedical Imaging: Nano to Macro, 2006. 3rd IEEE International Symposium on, pp. 698–701, 2006.
- [45] X. Qian, M. Brennan, D. Dione, W. Dobrucki, M. Jackowski, C. Breuer, A. Sinusas, X. Papademetris, A non-parametric vessel detection method for complex vascular structures, *Med. Image Anal.* 13 (2009) 49–61.
- [46] J. Schindelin, I. Arganda-Carreras, E. Frise, V. Kaynig, M. Longair, T. Pietzsch, S. Preibisch, C. Rueden, S. Saalfeld, B. Schmid, J.Y. Tinevez, D.J. White, V. Hartenstein, K. Eliceiri, P. Tomancak, A. Cardona, Fiji: an open-source platform for biological-image analysis, *Br. J. Pharmacol.* 9 (2012) 676–682.
- [47] L. Wang, G. Leedham, Gray-scale skeletonization of thermal vein patterns using the watershed algorithm in vein pattern biometrics, in: Computational Intelligence and Security, 2006 International Conference on, pp. 1597–1602, 2006.
- [48] F.C. Wu, W.C. Ma, P.C. Liou, R.H. Laing, M. Ouhyoung, Skeleton Extraction of 3d Objects with Visible Repulsive Force, 2003.
- [49] Z. Yu, C. Bajaj, A segmentation-free approach for skeletonization of gray-scale images via anisotropic vector diffusion, in: Computer Vision and Pattern Recognition, 2004. CVPR 2004. Proceedings of the 2004 IEEE Computer Society Conference on, pp. 415–420, 2004.
- [50] P.A. Yushkevich, J. Piven, H. Cody Hazlett, R. Gimpel Smith, S. Ho, J.C. Gee, G. Gerig, User-guided 3D active contour segmentation of anatomical structures: significantly improved efficiency and reliability, *Neuroimage* 31 (2006) 1116–1128.